

Reversible and cooperative photoactivation of single-atom Cu/TiO₂ photocatalysts

Byoung-Hoon Lee^{1,2,7}, Sunghak Park^{3,7}, Minh Kim⁴, Arun K. Sinha¹, Seong Chan Lee^{1,2}, Euiyeon Jung^{1,2}, Woo Je Chang³, Kug-Seung Lee⁵, Jeong Hyun Kim¹, Sung-Pyo Cho⁶, Hyungjun Kim^{4*}, Ki Tae Nam^{3*} and Taegwan Hyeon^{1,2*}

The reversible and cooperative activation process, which includes electron transfer from surrounding redox mediators, the reversible valence change of cofactors and macroscopic functional/structural change, is one of the most important characteristics of biological enzymes, and has frequently been used in the design of homogeneous catalysts. However, there are virtually no reports on industrially important heterogeneous catalysts with these enzyme-like characteristics. Here, we report on the design and synthesis of highly active TiO₂ photocatalysts incorporating site-specific single copper atoms (Cu/TiO₂) that exhibit a reversible and cooperative photoactivation process. Our atomic-level design and synthetic strategy provide a platform that facilitates valence control of co-catalyst copper atoms, reversible modulation of the macroscopic optoelectronic properties of TiO₂ and enhancement of photocatalytic hydrogen generation activity, extending the boundaries of conventional heterogeneous catalysts.

Heterogeneous photocatalysts have many potential applications including hydrogen production, CO₂ conversion, water treatment and organic synthesis^{1–4}. To achieve high efficiency and selectivity in these applications, the electronic band structures of the co-catalysts and their interactions with light absorbers should be investigated, along with the intrinsic light-absorbing properties of the photocatalysts^{5–10}. However, because the position and valence of co-catalysts are difficult to control at the atomic level, an atomistic understanding of the mechanism during photocatalysis remains elusive^{11,12}. In this regard, single-atom catalysts (SACs), in which isolated single atoms are anchored to the support, offer a representative platform because unique and enhanced catalytic performance can be achieved by tuning the local atomic configuration^{13–20}. Even in SACs, deterministic identification of the local atomic configuration and the corresponding catalytic process in dynamic reaction conditions is still challenging, especially for oxide-based SACs, which are typically synthesized by the impregnation method based on non-specific interactions^{13–15,18–20}. Here, we design and synthesize SACs with well-dispersed copper atoms that are exclusively occupied in the most stable Ti vacancies in hollow TiO₂ nanoparticles, and identify an atomic-level reversible and cooperative photoactivation process during dynamic photocatalysis.

Synthesized site-specific single-atom Cu/TiO₂ catalysts undergo a unique photoactivation process under the photocatalytic H₂ generation reaction condition (Fig. 1). Notably, the colour of the Cu/TiO₂ changes from white to black after light irradiation in a 3:1 (vol/vol) water/methanol solution under an Ar atmosphere (Fig. 1a). The black Cu/TiO₂ retains its colour even after the light is turned off under an Ar atmosphere, and efficiently generates H₂ under light irradiation. The colour reverts to the original white within a few minutes when exposed to O₂ without light irradiation, which completes the photoactivation cycle.

Figure 1b shows the photoactivation cycle. Initially, the single-atom Cu/TiO₂ is in a resting state, which is inactive (CT0 state). The CT0 state changes to a photoexcited state (CT1 state) by absorbing light, which generates electrons and holes. A photogenerated electron transfers from the conduction band of TiO₂ to the *d* orbital of the isolated copper atoms. The extra charge is compensated by oxygen protonation, resulting in a valence change of the redox-active isolated copper atoms (CT2 state). The trapped electron at the copper *d* orbital induces a polarization field, resulting in local TiO₂ lattice distortion around the isolated copper atoms (CT3 state). The resulting CT3 state has totally different photoelectrochemical properties and significantly enhanced photocatalytic H₂ generation activity. More importantly, the active CT3 state can be easily reverted to its original resting CT0 state when simply exposed to O₂ for a few minutes under dark conditions. This cooperative and reversible interaction between isolated copper atoms and the adjacent TiO₂ falls outside the boundaries of conventional heterogeneous catalysts and shares fundamental similarities with enzymes and related biomimetic homogeneous catalysts^{21–24}.

To synthesize site-specific SACs we first conducted density functional theory (DFT) studies to identify candidate binding sites to stabilize copper atoms on the TiO₂ anatase (101) surface and to determine the corresponding energetics associated with the binding process, enabling the design and synthesis of SACs exclusively in the vacancy aided binding sites (Fig. 2). We can simplify the formation energies of atomic catalysts (E_F) using the Born–Haber cycle, which includes the ‘binding site preparation energy’ for single atoms (E_p) and the ‘single atom binding energy’ of the prepared binding site (E_B): $E_F = E_p + E_B$ (Fig. 2b). Based on the calculated energy components, candidate sites can be classified into two groups: those that require E_p and those that do not (Fig. 2c). The three sites that do not

¹Center for Nanoparticle Research, Institute for Basic Science (IBS), Seoul, Republic of Korea. ²School of Chemical and Biological Engineering, and Institute of Chemical Processes, Seoul National University, Seoul, Republic of Korea. ³Department of Materials Science and Engineering, Seoul National University, Seoul, Republic of Korea. ⁴Department of Chemistry, Korea Advanced Institute of Science and Technology (KAIST), Daejeon, Republic of Korea.

⁵Pohang Accelerator Laboratory (PAL), Pohang University of Science and Technology (POSTECH), Pohang, Republic of Korea. ⁶National Center for Inter-University Research Facilities, Seoul National University, Seoul, Republic of Korea. ⁷These authors contributed equally: Byoung-Hoon Lee, Sunghak Park. *e-mail: linus16@kaist.ac.kr; nkitae@snu.ac.kr; thyeon@snu.ac.kr

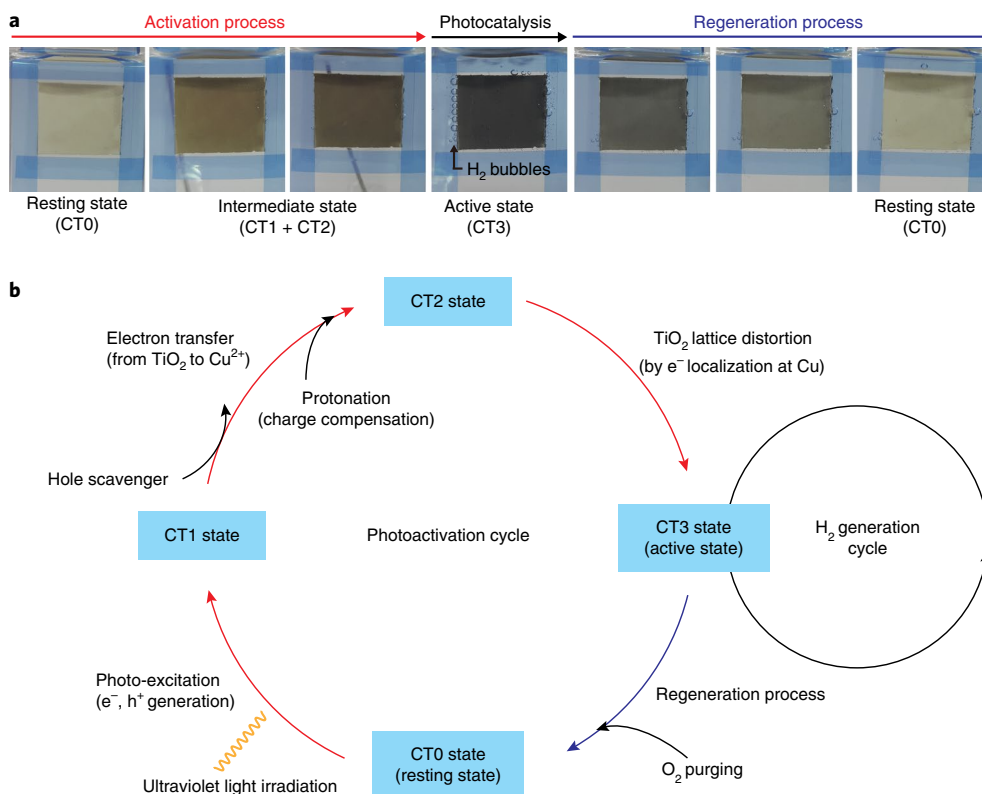


Fig. 1 | Cooperative photoactivation cycle of Cu/TiO₂. **a**, Photographs of Cu/TiO₂ film in various states of photoactivation cycle. **b**, Photoactivation cycle of Cu/TiO₂.

require E_p (atop Ti site, hollow site and bridge site) are classified as ‘surface binding sites’, while the two binding sites that do require E_p (O vacancy and Ti vacancy) are classified as ‘vacancy aided binding sites’ that require high external energy for vacancy formation. Our DFT results suggest that the synthesis must be controlled by a thermodynamic driving force to ensure binding in Ti vacancies rather than O vacancies. We therefore used a modified wrap–bake–peel process²⁵, which involves coating with a silica overlayer to prevent surface diffusion and allows for high-temperature heat treatment, which is necessary to incorporate metal atoms exclusively in the most stable Ti vacancies on TiO₂. The synthetic procedure for the modified wrap–bake–peel process comprises the following steps (Fig. 2d and Supplementary Figs. 1–4): (1) sol–gel coating of TiO₂ on silica spheres, followed by adsorption of the metal precursor; (2) coating with a silica overlayer (wrap); (3) heat treatment at 900 °C (bake); (4) etching of the silica (peel).

Low- and high-resolution transmission electron microscopy (HRTEM) images show that well-dispersed Cu/TiO₂ nanoparticles consist of ~5nm TiO₂ nanocrystals (Fig. 3a,b), whereas severe agglomeration is observed without the SiO₂ protection (Supplementary Fig. 5). Energy-dispersive X-ray spectroscopy (EDS) analysis in scanning transmission electron microscopy (STEM) mode shows a homogeneous dispersion of copper species without agglomeration (Fig. 3c). These findings are further supported by X-ray diffraction (XRD) analysis, in which no diffraction pattern except that of TiO₂ is observed (Supplementary Fig. 6).

X-ray absorption near-edge structure (XANES) spectroscopy shows an absorption edge energy at 8,996.3 eV and a small shoulder at 8,989.3 eV in the initial white Cu/TiO₂ film, which are typical characteristics of Cu²⁺ (Fig. 3d). The Ti K edge spectrum in extended X-ray-absorption fine-structure (EXAFS) analysis reveals the presence of two characteristic distances of Ti–O and Ti–Ti in

the crystalline anatase phase (Fig. 3e). The EXAFS spectrum of the Cu K edge is very similar to that of the Ti K edge (Fig. 3e), indicating that the metal atoms are located in the Ti sites, and no characteristic peak corresponding to metallic bonding is observed, as corroborated by the XRD data. The site-specific configuration results in a main peak corresponding to the direct binding of copper atoms and lattice oxygen (Cu–O), as well as a minor peak indicating the local TiO₂ environment (Cu–Ti) around the isolated copper. The local coordination environment was then investigated by EXAFS curve-fitting analysis. The best-fit curve in Fig. 3e shows that the first peak originates from the first Cu–O shell coordination, whereas the minor second peak originates from the Cu–Ti contribution (Fig. 3e and Supplementary Figs. 7 and 8).

This modified wrap–bake–peel process can be generalized to produce SACs that are highly loaded with various atomically dispersed metals, including Co, Fe, Ni, Cu and Rh, exclusively in the Ti vacancies of hollow TiO₂ nanoparticles (Supplementary Figs. 6–13 and Supplementary Table 1). We performed high-angle annular dark-field (HAADF) STEM studies on the Rh/TiO₂ sample, which was chosen for direct imaging of the local structure of isolated metal atoms because Rh exhibits a much stronger contrast than Ti (Fig. 3f–j and Supplementary Figs. 14–18). Bright contrast spots are located only on the Ti atomic row, confirming that Rh atoms are exclusively present in the Ti vacancies (Fig. 3g,h,j). Other Rh configurations are not detected (Supplementary Figs. 14–18). Using electron energy loss spectroscopy (EELS), we further verified that the bright contrast spots are indeed single Rh atoms (Supplementary Fig. 18). The atomic-resolution HAADF-STEM imaging and EXAFS analysis results are consistent, confirming the homogeneous incorporation of metal atoms in site-specific Ti vacancies.

We performed the photocatalytic H₂ generation reaction as a model reaction using methanol as a hole scavenger (Fig. 4a,b).

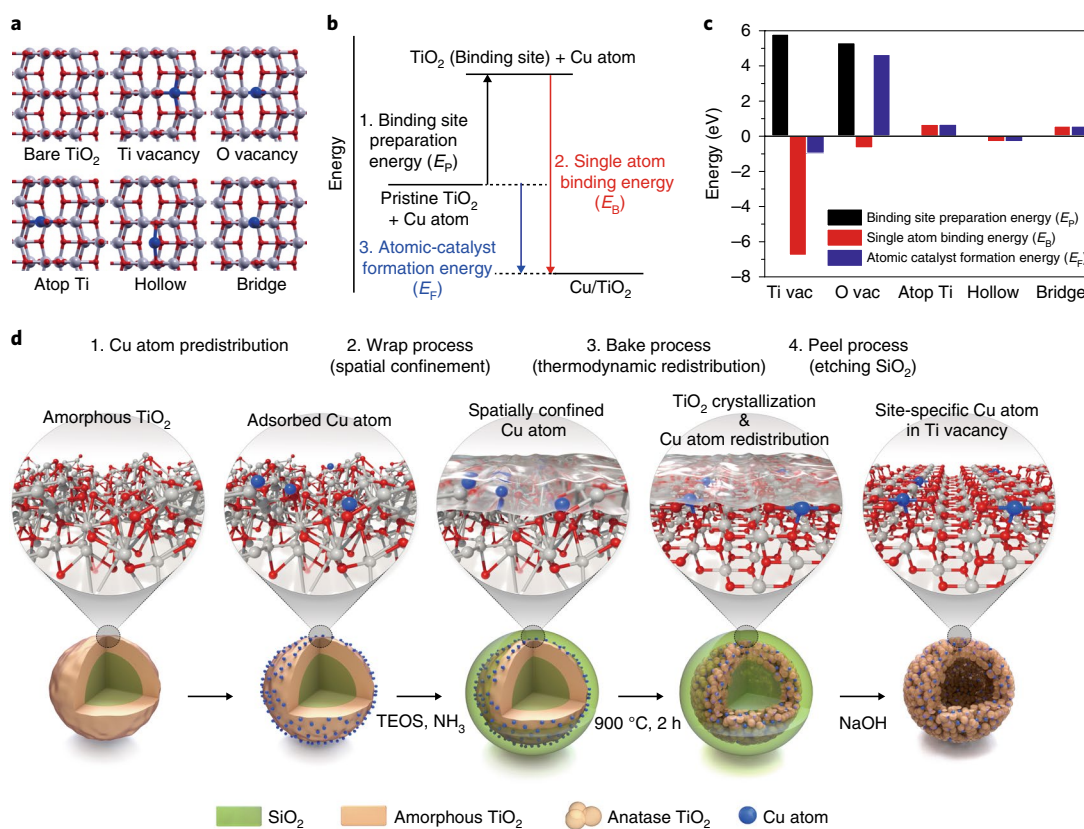


Fig. 2 | Designing a site-specific single-atom photocatalyst. **a**, Candidate binding sites for single metal atoms on a TiO₂ anatase (101) surface. **b**, Born-Haber thermodynamic cycle for calculating SAC formation energies (E_f): the binding site preparation energy (E_p) + the single atom binding energy (E_b). **c**, Born-Haber energy components for possible single-atom binding sites calculated using DFT. **d**, Modified wrap-bake-peel process to synthesize single-atom Cu/TiO₂ photocatalysts. TEOS, tetraethyl orthosilicate.

All the synthesized SACs incorporated with Co, Fe, Ni, Cu and Rh (metal loading of 0.75 wt%) showed an enhanced photocatalytic H₂ production rate compared to pure TiO₂ (Fig. 4a). Cu/TiO₂ and Rh/TiO₂ exhibited 34.0 and 26.6 times higher photocatalytic activities than that of pure TiO₂, respectively. Consequently, we chose the Cu/TiO₂ SACs for further photocatalytic studies. By introducing a very small amount of copper (0.05 wt%), the H₂ production rate (2.36 mmol g⁻¹ h⁻¹) significantly increased by a factor of 4.8 compared to that of pure TiO₂ (Supplementary Fig. 19). At 0.75 wt% Cu/TiO₂, the H₂ production rate reached its highest value of 16.6 mmol g⁻¹ h⁻¹ (Fig. 4b); H₂ production was stable without any noticeable decrease in photocatalytic activity over four successive cycles (Fig. 4c). The optimized 0.75 wt% Cu/TiO₂ shows an apparent quantum efficiency (AQE) of 45.5% at 340 nm, far exceeding that of the state-of-the-art TiO₂-based photocatalysts incorporated with earth-abundant transition metal-based co-catalysts (AQE of 4.3–17.2%, Supplementary Table 2). Under visible light irradiation (400 nm cut-on filter), the activated CT3 state sample exhibited a moderate H₂ production rate of 3.73 μmol g⁻¹ h⁻¹, even without the Pt co-catalyst.

As revealed by the difference in colour between the resting state sample and the active state sample, UV-vis absorption spectra show totally different patterns (Fig. 4d). Resting state CT0 sample showed a sharp onset at ~390 nm and a broad band at 700 nm, which correspond to the band-to-band transition of anatase TiO₂ and the *d-d* transition of Cu, respectively (black curve in Fig. 4d). Active state CT3 sample exhibits very strong absorption in the whole range of measured wavelengths (300–800 nm) (red curve in Fig. 4d). This strong absorption in the whole visible region is extraordinary, even compared to the intensively studied black TiO₂ materials synthesized under harsh conditions (for example, 20 bar H₂ atmosphere at 200 °C for 5 days) to

induce irreversible structural distortion^{26–30}. In contrast, our sample was in situ generated by the reversible photoactivation process without any harsh reaction conditions, which can easily be reversed.

Photocatalytic activity is closely related to the status of the sample. The rate of H₂ evolution rapidly increased during the first 10 min of light irradiation and remained nearly constant afterwards (Fig. 4e). This timescale of activation of the H₂ production rate (~10 min) matches well with that of the colour change of the film. Furthermore, photoluminescence spectroscopy was performed to check the recombination rate of photogenerated charge carriers. Interestingly, the photoluminescence spectrum of the initial resting CT0 state (black line, Fig. 4f) is almost identical to that of bare TiO₂ (blue line, Fig. 4f), showing that efficient separation of charge carriers does not occur before light activation. The photoluminescence spectra of the active CT3 state (red line, Fig. 4f) significantly decreased, revealing that the initial white Cu/TiO₂ (CT0, resting state) is dormant and that the in situ generated black Cu/TiO₂ (CT3, active state) is responsible for the exceptional photocatalytic activity.

The valence state change of isolated copper during the photoactivation cycle was revealed by XANES measurements. After irradiation of the CT0 state sample, a distinct shoulder developed at 8,982.1 eV and the main peak at 8,996.3 eV decreased (Fig. 5a), showing that the valence of the copper is reduced by photogenerated electrons. When the CT3 state sample was exposed to O₂ to regenerate the CT0 state, XANES spectra recovered to its original shape, as shown in Fig. 5b.

To further elucidate the change in the oxidation states of both Cu and Ti during the photoactivation cycle, low-temperature electron paramagnetic resonance (EPR) spectra were obtained (Fig. 5c and Supplementary Fig. 20). From the EPR spectra, the proportionality factor (*g*-factor) can be obtained, which is the unique property of

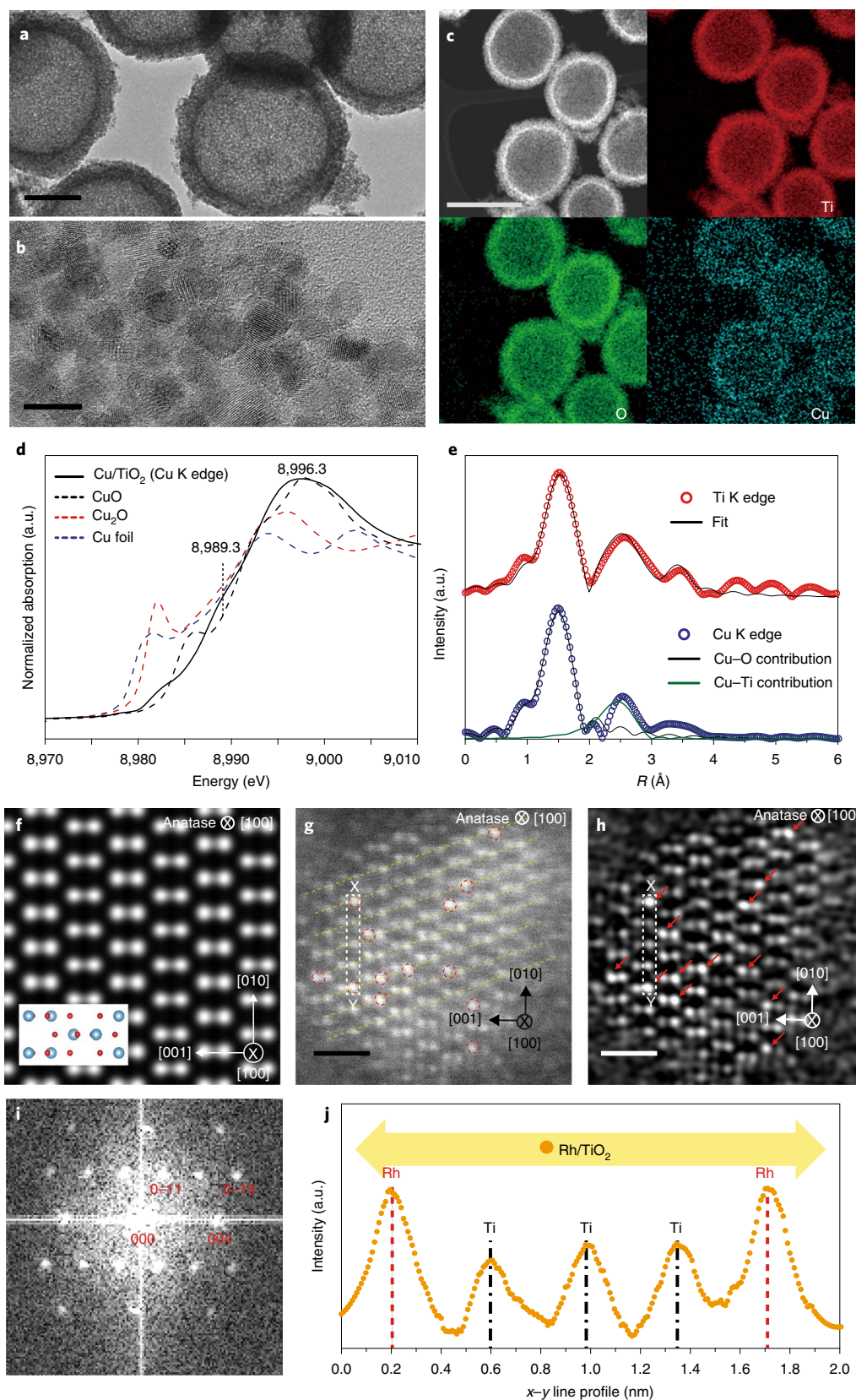


Fig. 3 | Characterization of single-atom catalysts. **a, b**, Representative low (**a**) and high (**b**) magnification TEM images of Cu/TiO₂. Scale bars, 100 nm (**a**), 10 nm (**b**). **c**, STEM-EDS elemental mapping of Cu/TiO₂. Scale bar, 250 nm. **d**, Cu K-edge XANES spectra of Cu/TiO₂. **e**, EXAFS spectra and analysis of Cu/TiO₂ at Ti and Cu K-edges. **f–i**, Atomic-level characterization of Rh/TiO₂ in the [100] direction: simulated HAADF-STEM image of anatase TiO₂ (**f**) (inset shows corresponding unit cell structure of anatase TiO₂); Cs-corrected HAADF STEM raw image (**g**) and filtered image (**h**) and corresponding fast Fourier transform pattern (**i**) of Rh/TiO₂. Blue and red balls in inset of **f** represent Ti and O atoms, respectively. Isolated Rh atoms in Ti vacancies are marked as dashed circles in **g** and arrows in **h**. **j**, x–y line scan profile, measured from **g**.

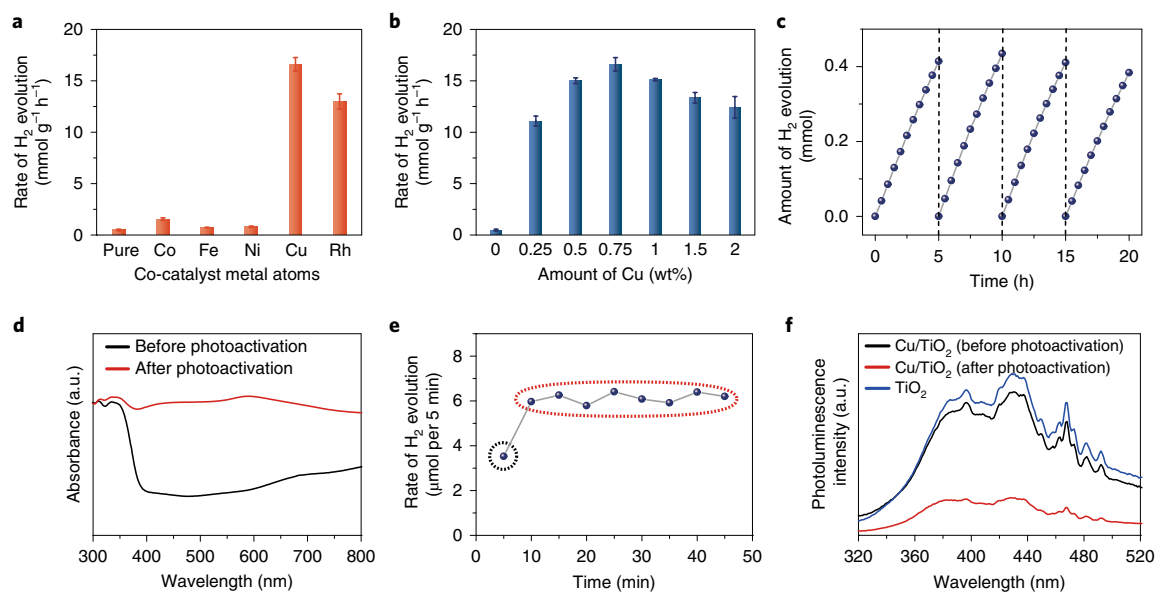


Fig. 4 | Photocatalytic H_2 generation activity and spectroscopic characterization of Cu/TiO_2 . **a**, Rate of photocatalytic H_2 generation of M/TiO_2 (0.75 wt%) for each type of co-catalyst. **b**, Rate of photocatalytic H_2 generation of Cu/TiO_2 depending on the loading amount of Cu. Error bars in **a** and **b** are standard error values of three tests ($n=3$). **c**, Cyclic measurements of photocatalytic H_2 generation of Cu/TiO_2 (0.75 wt%), showing the stable activity. **d**, Spectral absorbance change of Cu/TiO_2 before (black line) and after (red line) 10 min of light irradiation (0.75 wt% Cu/TiO_2 sample). **e**, Comparison of the photocatalytic H_2 evolution rate of Cu/TiO_2 in the first 5 min (black dotted circle) and afterwards (red dotted ellipse). **f**, Photoluminescence spectra of bare TiO_2 (blue line) and Cu/TiO_2 before (black line) and after (red line) 10 min of light irradiation.

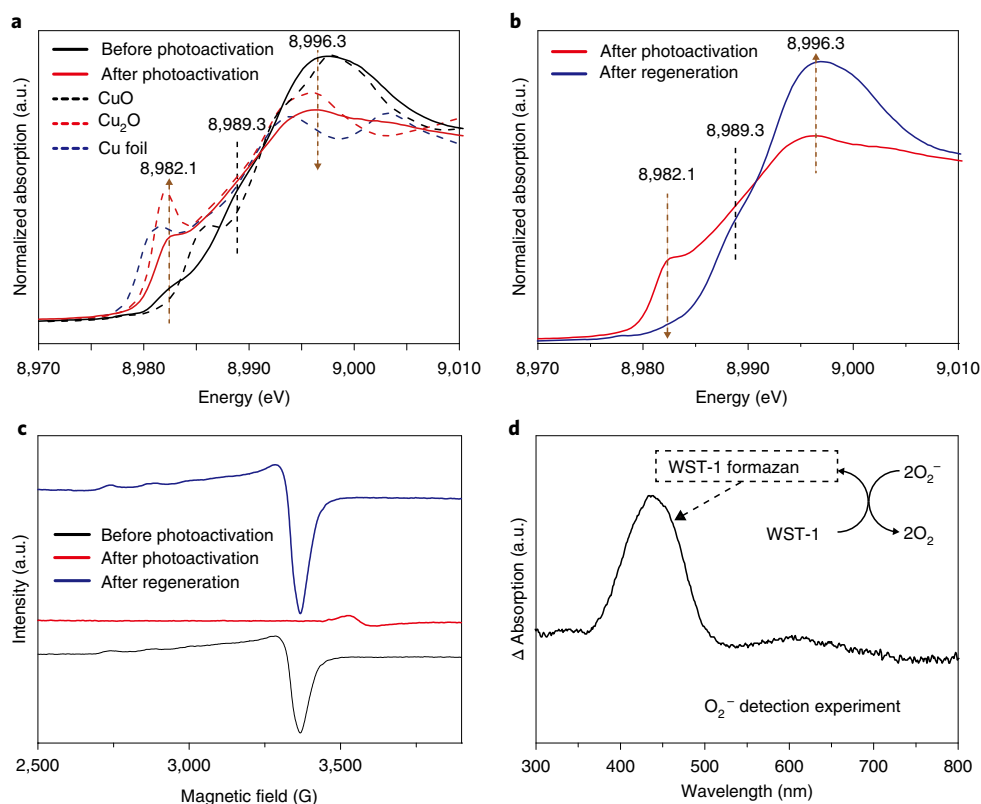


Fig. 5 | Characterization of the Cu/TiO_2 photoactivation cycle mechanism through spectroscopic analysis **a**, Cu K-edge XANES spectra of Cu/TiO_2 before (black line, identical to Fig. 3d) and after (red line) 10 min of light irradiation. **b**, Cu K-edge XANES spectra of Cu/TiO_2 after photoactivation (red line) and after regeneration (blue line) by O_2 purging. **c**, Low temperature X-band EPR spectra of Cu/TiO_2 in various states. **d**, Difference in absorbance spectra between the WST-1 solution with resting Cu/TiO_2 and the WST-1 solution with Cu/TiO_2 regenerated by O_2 purging.

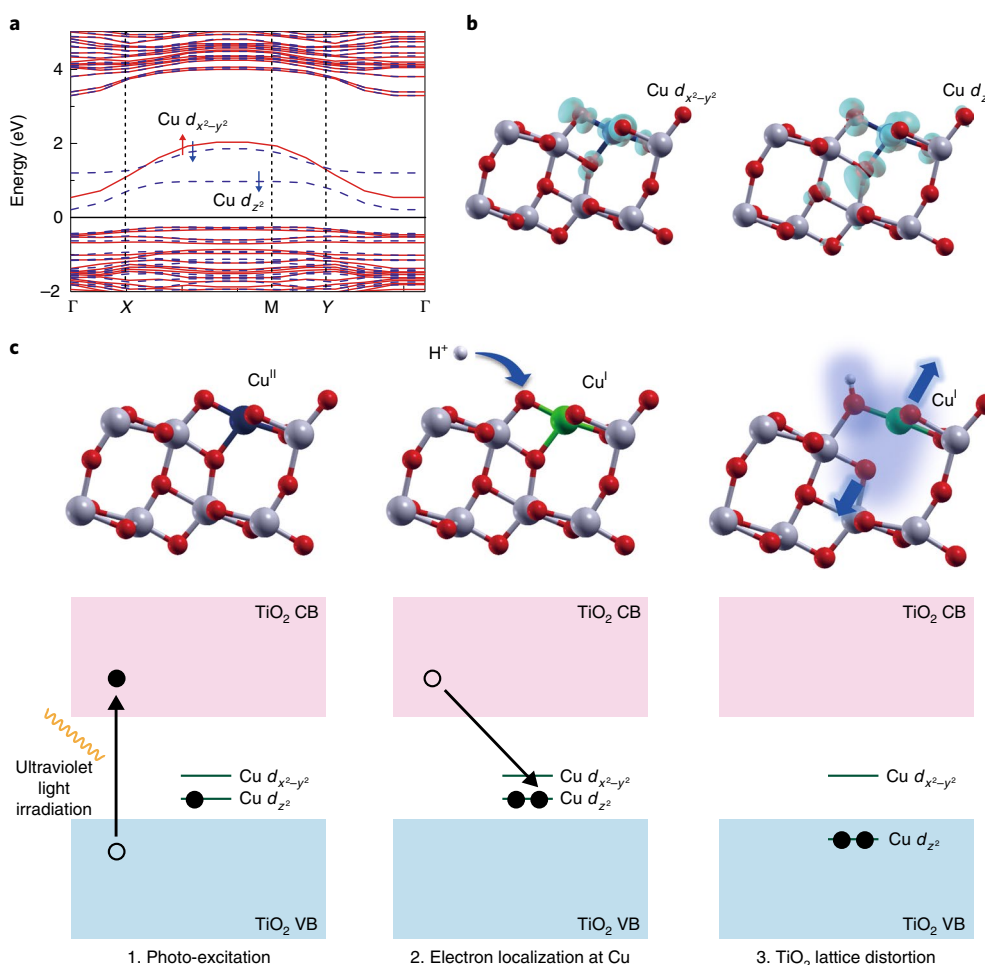


Fig. 6 | Role of isolated Cu atoms in the cooperative interplay of Cu and TiO₂. **a**, DFT-calculated band structure of Cu/TiO₂ with the Fermi level set to zero, and the band-decomposed partial charge density of the mid-gap states. The red solid line and the blue dashed line show the up and down spin states (marked as red and blue arrows) for each band, respectively. **b**, Atomic structure of Cu/TiO₂ showing $d_{x^2-y^2}$ (left) and d_{z^2} (right) orbitals of the Cu atom. **c**, Schematics of the photo-excitation process of photo-electron generation (left), its localization to the Cu d_{z^2} antibonding state along with surface protonation (middle) and local structural distortion (right). The top panels show the DFT-optimized structure for each step. VB, valence band; CB, conduction band.

the electron in a certain environment. The EPR spectrum of the initial CT0 state sample exhibited a characteristic Cu²⁺ signal ($g_{\parallel} = 2.33$, $g_{\perp} = 2.07$)³¹. After the photoactivation process, the CT3 state sample shows two distinct changes in the EPR spectra. First, the characteristic Cu²⁺ signal has completely disappeared. The EPR and XANES results reveal that Cu²⁺ is reduced to EPR-silent Cu¹⁺ during the photoactivation process. Second, a new small signal has appeared at $g_{\text{eff}} = 1.93$, which matches well with the previously reported paramagnetic Ti³⁺ centre³². When the CT3 state sample was exposed to O₂ for regeneration, the EPR spectra reverted to the initial CT0 spectra.

The reduction product of O₂ during the regeneration process was analysed with colorimetric analysis. Because O₂ acts as an oxidant to oxidize the CT3 state sample, the possible O₂ products can be superoxide, peroxide and H₂O. Water-soluble tetrazolium salt (WST-1) and titanium(IV) sulfate were used to detect superoxide and peroxide, respectively^{33,34}. As shown in Fig. 5d and Supplementary Fig. 21, superoxide was detected, but peroxide was not, suggesting that the regeneration process occurs through single electron transfer between molecular O₂ and the surface of the CT3 sample. Taken together, all Cu atoms are reduced from Cu²⁺ to Cu¹⁺, and a small number of Ti atoms are simultaneously reduced from Ti⁴⁺ to Ti³⁺ by the electrons photogenerated during the photoactivation process. More interestingly, when exposed to O₂, spectroscopic data for the CT3 state sample fully revert to the original CT0 state along with the superoxide generation.

DFT calculations using hybrid functionals can give important insights when predicting the accurate electronic structures of TiO₂ (refs. 35–37). Hybrid DFT calculations further elucidate that the Cu atom in a Ti vacancy provides mid-gap states with Cu $d_{x^2-y^2}$ and d_{z^2} character in between the valence and conduction bands of TiO₂ (Fig. 6a,b). After photo-excitation (Fig. 6c, left), the photogenerated electron is localized into the Cu d_{z^2} state and changes the valence state of the Cu atom (Supplementary Fig. 22a), where an additional proton needs to be adsorbed on the surface to balance the surface charge (Fig. 6c, middle). It is interesting to note that the photogenerated electron of the pure TiO₂ surface remains delocalized in the conduction band of TiO₂, rather than being localized at the metal centre due to the absence of the Cu redox centre (Supplementary Fig. 22b). Because the Cu d_{z^2} state has an axial antibonding character, electron localization at this state leads to a lattice distortion by elongating the back-side oxygen coordination from 1.959 Å to 2.113 Å (Fig. 6c, right), which not only stabilizes the localized electron at Cu, but also causes lattice distortion in nearby TiO₂. Consequently, we can conclude that isolated copper acts as a redox-active metal cofactor that reversibly tunes the local TiO₂ lattice during the dynamic photocatalysis.

In summary, these experimental results and DFT studies provide insight into how isolated copper atoms affect the overall photocatalytic reaction. During the dynamic photocatalytic process, the valence state of the isolated Cu atoms is changed by the

atomistic localization of photogenerated electrons. This valence change induces activation of adjacent TiO₂, thereby tuning the initially dormant TiO₂ to an active state that significantly enhances photocatalytic performance (Supplementary Fig. 23). Our results show that a reversible and cooperative activation process occurs at the single-atom level and enables the control of macroscopic optoelectronic properties and subsequent enhancement of catalytic activity. Furthermore, we demonstrate that the cooperative interplay of atomic catalysts and adjacent environments has a significant influence on the overall material properties and catalytic activity, implying that atomic-level cooperative interaction shares fundamental similarities with metalloenzymes and homogeneous catalysts, which has been overlooked in heterogeneous catalysts.

Online content

Any methods, additional references, Nature Research reporting summaries, source data, extended data, supplementary information, acknowledgements, peer review information; details of author contributions and competing interests; and statements of data and code availability are available at <https://doi.org/10.1038/s41563-019-0344-1>.

Received: 17 August 2018; Accepted: 15 March 2019;

Published online: 22 April 2019

References

- Hisatomi, T., Kubota, J. & Domen, K. Recent advances in semiconductors for photocatalytic and photoelectrochemical water splitting. *Chem. Soc. Rev.* **43**, 7520–7535 (2014).
- Hoffmann, M. R., Martin, S. T., Choi, W. & Bahnemann, D. W. Environmental applications of semiconductor photocatalysis. *Chem. Rev.* **95**, 69–96 (1995).
- Kudo, A. & Miseki, Y. Heterogeneous photocatalyst materials for water splitting. *Chem. Soc. Rev.* **38**, 253–278 (2009).
- Montoya, J. H. et al. Materials for solar fuels and chemicals. *Nat. Mater.* **16**, 70–81 (2017).
- Cargnello, M. et al. Engineering titania nanostructure to tune and improve its photocatalytic activity. *Proc. Natl Acad. Sci. USA* **113**, 3966–3971 (2016).
- Gordon, T. R. et al. Nonaqueous synthesis of TiO₂ nanocrystals using TiF₄ to engineer morphology, oxygen vacancy concentration and photocatalytic activity. *J. Am. Chem. Soc.* **134**, 6751–6761 (2012).
- Choi, W., Termin, A. & Hoffmann, M. R. The role of metal ion dopants in quantum-sized TiO₂: correlation between photoreactivity and charge carrier recombination dynamics. *J. Phys. Chem.* **98**, 13669–13679 (1994).
- Ran, J., Zhang, J., Yu, J., Jaroniec, M. & Qiao, S. Z. Earth-abundant cocatalysts for semiconductor-based photocatalytic water splitting. *Chem. Soc. Rev.* **43**, 7787–7812 (2014).
- Yang, H. G. et al. Anatase TiO₂ single crystals with a large percentage of reactive facets. *Nature* **453**, 638–641 (2008).
- Park, S. et al. Photocatalytic hydrogen generation from hydriodic acid using methylammonium lead iodide in dynamic equilibrium with aqueous solution. *Nat. Energy* **2**, 16185 (2016).
- Guo, Q. et al. Elementary photocatalytic chemistry on TiO₂ surfaces. *Chem. Soc. Rev.* **45**, 3701–3730 (2016).
- Hussain, H. et al. Structure of a model TiO₂ photocatalytic interface. *Nat. Mater.* **16**, 461–466 (2017).
- Wang, A., Li, J. & Zhang, T. Heterogeneous single-atom catalysis. *Nat. Rev. Chem.* **2**, 65–81 (2018).
- Qiao, B. et al. Single-atom catalysis of CO oxidation using Pt/FeO_x. *Nat. Chem.* **3**, 634–641 (2011).
- Liu, P. et al. Photochemical route for synthesizing atomically dispersed palladium catalysts. *Science* **352**, 797–800 (2016).
- Lin, L. et al. Low-temperature hydrogen production from water and methanol using Pt/α-MoC catalysts. *Nature* **544**, 80–83 (2017).
- Choi, C. H. et al. Tuning selectivity of electrochemical reactions by atomically dispersed platinum catalyst. *Nat. Commun.* **7**, 10922 (2016).
- Shan, J., Li, M., Allard, L. F., Lee, S. & Flytzani-Stephanopoulos, M. Mild oxidation of methane to methanol or acetic acid on supported isolated rhodium catalysts. *Nature* **551**, 605–608 (2017).
- Nie, L. et al. Activation of surface lattice oxygen in single-atom Pt/CeO₂ for low-temperature CO oxidation. *Science* **358**, 1419–1423 (2017).
- DeRita, L. et al. Catalyst architecture for stable single atom dispersion enables site-specific spectroscopic and reactivity measurements of CO adsorbed to Pt atoms, oxidized Pt clusters, and metallic Pt clusters on TiO₂. *J. Am. Chem. Soc.* **139**, 14150–14165 (2017).
- Benkovic, S. J. & Hammes-Schiffer, S. A perspective on enzyme catalysis. *Science* **301**, 1196–1202 (2003).
- Liu, J. et al. Metalloproteins containing cytochrome, iron–sulfur, or copper redox centers. *Chem. Rev.* **114**, 4366–4469 (2014).
- Que, L. Jr & Tolman, W. B. Biologically inspired oxidation catalysis. *Nature* **455**, 333–340 (2008).
- Wodrich, M. D. & Hu, X. Natural inspirations for metal–ligand cooperative catalysis. *Nat. Rev. Chem.* **2**, 0099 (2017).
- Piao, Y. et al. Wrap–bake–peel process for nanostructural transformation from β-FeOOH nanorods to biocompatible iron oxide nanocapsules. *Nat. Mater.* **7**, 242 (2008).
- Chen, X., Liu, L., Peter, Y. Y. & Mao, S. S. Increasing solar absorption for photocatalysis with black hydrogenated titanium dioxide nanocrystals. *Science* **331**, 746–750 (2011).
- Chen, X., Liu, L. & Huang, F. Black titanium dioxide (TiO₂) nanomaterials. *Chem. Soc. Rev.* **44**, 1861–1885 (2015).
- Jung, D. et al. A molecular cross-linking approach for hybrid metal oxides. *Nat. Mater.* **17**, 341–348 (2018).
- Selcuk, S., Zhao, X. & Selloni, A. Structural evolution of titanium dioxide during reduction in high-pressure hydrogen. *Nat. Mater.* **17**, 923–928 (2018).
- Zhou, W. et al. Ordered mesoporous black TiO₂ as highly efficient hydrogen evolution photocatalyst. *J. Am. Chem. Soc.* **136**, 9280–9283 (2014).
- Neubert, S. et al. Highly efficient rutile TiO₂ photocatalysts with single Cu(II) and Fe(III) surface catalytic sites. *J. Mater. Chem. A* **4**, 3127–3138 (2016).
- Siemer, N. et al. Atomic scale explanation of O₂ activation at the Au–TiO₂ interface. *J. Am. Chem. Soc.* **140**, 18082–18092 (2018).
- Hayyan, M., Hashim, M. A. & AlNashef, I. M. Superoxide ion: generation and chemical implications. *Chem. Rev.* **116**, 3029–3085 (2016).
- Kim, J. et al. Continuous O₂-evolving MnFe₂O₄ nanoparticle-anchored mesoporous silica nanoparticles for efficient photodynamic therapy in hypoxic cancer. *J. Am. Chem. Soc.* **139**, 10992–10995 (2017).
- Krukau, A. V., Vydrov, O. A., Izmaylov, A. F. & Scuseria, G. E. Influence of the exchange screening parameter on the performance of screened hybrid functionals. *J. Chem. Phys.* **125**, 224106 (2006).
- Finazzi, E., Valentin, C. D., Pacchioni, G. & Selloni, A. Excess electron states in reduced bulk anatase TiO₂: comparison of standard GGA, GGA + U and hybrid DFT calculations. *J. Chem. Phys.* **129**, 154113 (2008).
- Setvín, M. et al. Reaction of O₂ with subsurface oxygen vacancies on TiO₂ anatase (101). *Science* **341**, 988–991 (2013).

Acknowledgements

Synthesis and physicochemical property analysis of the nanomaterial samples were supported by the Research Center Program of the IBS (IBS-R006-D1) in Korea (T.H.). Photocatalytic analysis was supported by the Creative Materials Discovery Program through the National Research Foundation of Korea (NRF) funded by the Ministry of Science and ICT (NRF-2017M3D1A1039377). Computational work was supported by the Creative Materials Discovery Program (grant no. 2017M3D1A1039378) funded by the Korea government (MSIT). X-ray absorption spectroscopy work was supported by the Nano-Material Fundamental Technology Development programme (NRF-2018R1D1A1B07041997) through the NRF. The authors also thank the Korean Basic Science Institute (KBSI) at the Western Seoul Center for help with EPR measurements.

Author contributions

B.-H.L., S.P., H.K., K.T.N. and T.H. conceived the research. B.-H.L. and S.P. designed the experiments. B.-H.L., A.K.S., S.C.L. and E.J. performed and analysed the results. S.P., B.-H.L. and W.J.C. performed photochemical reactions. M.K. and H.K. performed the DFT calculations and analysis. S.-P.C. conducted the HAADF-STEM and EELS analysis. K.-S.L. contributed to the X-ray absorption spectroscopy experiments and analysis. B.-H.L., S.P., M.K., J.H.K., H.K., K.T.N. and T.H. wrote the manuscript. H.K., K.T.N. and T.H. supervised the project. All authors commented on the manuscript.

Competing interests

The authors declare no competing interests.

Additional information

Supplementary information is available for this paper at <https://doi.org/10.1038/s41563-019-0344-1>.

Reprints and permissions information is available at www.nature.com/reprints.

Correspondence and requests for materials should be addressed to H.K., K.T.N. or T.H.

Publisher's note: Springer Nature remains neutral with regard to jurisdictional claims in published maps and institutional affiliations.

© The Author(s), under exclusive licence to Springer Nature Limited 2019

Methods

Materials. All reagents were used as received without further purification. Titanium(IV) *n*-butoxide (TBOT) was purchased from Strem Chemicals. Iron(III) chloride hexahydrate (FeCl₃·6H₂O), cobalt(II) chloride trihydrate (CoCl₂·3H₂O), nickel(II) chloride hexahydrate (NiCl₂·6H₂O), copper(II) chloride dihydrate (CuCl₂·2H₂O), rhodium(III) chloride hydrate (RhCl₃·xH₂O), TEOS and polyvinylpyrrolidone (PVP) ($M_w = 55,000$) were purchased from Sigma Aldrich. Acetonitrile, anhydrous ethyl alcohol (purity = 99.9%), sodium hydroxide (NaOH) and ammonia solution (28–30 wt%) were purchased from Samchun Chemical.

Synthesis of M/TiO₂. *Synthesis of silica nanoparticles.* Spherical silica (SiO₂) nanoparticles were synthesized by sol–gel reaction in a basic environment following the previously reported Stöber method. A 0.86 ml volume of TEOS was added to a solution containing ethyl alcohol (23 ml), H₂O (4.3 ml) and aqueous ammonia (0.6 ml) at room temperature. The mixture was then vigorously stirred for 6 h. Reaction products were centrifuged, washed with water and ethyl alcohol, and dispersed in ethyl alcohol.

Coating SiO₂ nanoparticles with TiO₂ (SiO₂@TiO₂). SiO₂ particles were coated with TiO₂ following a previously described method³⁸ with modifications. Prepared SiO₂ particles were dispersed in 40 ml of anhydrous ethyl alcohol. Then, 14 ml of pure acetonitrile and 0.4 ml of ammonia (28–30 wt%) were mixed with the SiO₂ nanoparticle solution, which is referred to as solution 1. The amount of aqueous ammonia in solution 1 critically affects the kinetics of the TiO₂ coating. Solution 1 was sonicated for at least 10 min to obtain well-dispersed SiO₂ nanoparticles. Meanwhile, 0.8 ml of TBOT was dissolved in a mixture containing 6 ml of anhydrous ethyl alcohol and 2 ml of acetonitrile (solution 2). Solution 2 was added to solution 1 and stirred for 3 h to coat the TiO₂. The resulting white solution was centrifuged and washed with ethanol and water twice, respectively. Finally, SiO₂@TiO₂ nanoparticles were dispersed in 40 ml of H₂O.

Transition metal atom adsorption on SiO₂@TiO₂ nanoparticles (SiO₂@M/TiO₂). Metal chloride hydrates (FeCl₃·6H₂O, CoCl₂·3H₂O, NiCl₂·6H₂O, CuCl₂·2H₂O and RhCl₃·xH₂O) were used as the metal precursors. In this metal atom adsorption process, a calculated amount of metal chloride (4.0 mg) was added into the previously prepared 40 ml colloidal solution of SiO₂@TiO₂ nanoparticles. Subsequently, the mixed colloidal solution was vigorously stirred for 3 h at room temperature. After stirring, the resulting material (SiO₂@M/TiO₂) was separated and washed with water by centrifugation. The metal ion adsorption changed the colour of the resulting material (SiO₂@M/TiO₂) from white to that of the adsorbed metal ion (FeCl₃·6H₂O, yellow; CoCl₂·3H₂O, blue; NiCl₂·6H₂O, green; CuCl₂·2H₂O, light blue; RhCl₃·xH₂O, orange).

Wrap process for coating SiO₂ on SiO₂@M/TiO₂ nanoparticles (SiO₂@M/TiO₂@SiO₂). The above SiO₂@M/TiO₂ nanoparticles were dispersed in 40 ml of H₂O. After adding PVP (0.4 g), the solution was stirred overnight to allow adsorption of PVP onto the surface of the SiO₂@M/TiO₂ nanoparticles. After PVP adsorption, the product was separated by centrifugation and redispersed in a solution of ethanol (46 ml) and H₂O (8.6 ml) by strong sonication for 10 min. A 1.2 ml volume of aqueous ammonia (28–30 wt%) and 1.6 ml of TEOS were then added to the above solution. The instantaneous stabilization of metal atoms adsorbed on the surface caused a rapid colour change within 10 s, followed by the formation of the SiO₂ overlayer. After 4 h of reaction, the resulting nanoparticles were washed with ethanol and water. The products were centrifuged, dried in air at 80 °C overnight and ground in a mortar to achieve uniformity.

Redistribution of metal atoms (SiO₂@M/TiO₂@SiO₂) bake process. To spatially confine the redistribution of metal atoms, the dry SiO₂@M/TiO₂@SiO₂ nanoparticle powders were calcined at 900 °C for 2 h. The annealing was conducted in open air to supply sufficient oxygen for the redistribution process.

Etching SiO₂ to prepare M/TiO₂ hollow nanoparticles (M/TiO₂ HNP) peel process. For SiO₂ etching, calcined SiO₂@M/TiO₂@SiO₂ nanoparticles were dispersed in a 0.5 M NaOH solution. The dispersion was then heated to 90 °C with continuous stirring. After 6 h, the product was separated by centrifugation and washed with H₂O and ethyl alcohol to yield the M/TiO₂ solution. The products were dried in an electric oven at 80 °C overnight and used for characterization and/or photocatalytic reactions.

Preparation of bulk Cu/TiO₂ reference. To fabricate the bulk Cu/TiO₂ reference, the synthesis was performed in the same manner as for M/TiO₂ HNP synthesis, as described in the previous section, but without using SiO₂ as a template or coating layer. First, TiO₂ was formed by a hydrolysis reaction, followed by Cu ion adsorption onto the TiO₂ surface and annealing at 900 °C for 2 h in air. The synthesized Cu/TiO₂ reference was used for further characterization and/or photocatalytic reactions.

Characterization of M/TiO₂. *Electron microscopy measurements.* TEM imaging was conducted on a JEOL EM-2010 microscope operated at 200 kV. EDS measurements

were performed in STEM mode equipped with a single drift detector (X-Max^N, Oxford Instruments). Field emission scanning electron microscopy imaging was conducted on a JEOL JSM-7800F-Prime microscope operated at 30 kV. The powder samples were deposited on a carbon tape and subsequently coated with platinum to increase conductivity before characterization. EDS data were also collected for bulk Cu/TiO₂ samples in SEM mode.

Atomic-resolution imaging on Cs-corrected STEM. Atomic-resolution imaging of Rh/TiO₂ was performed using a spherical aberration-corrected JEM ARM-200F microscope (Cold FEG Type, JEOL) equipped with an EELS detector (965 GIF Quantum ER, GATAN), installed at the National Center for Inter-University Research Facilities (NCIRF) at Seoul National University. The Rh/TiO₂ sample was chosen for the analysis because only Rh exhibits a much stronger contrast than Ti in Z-contrast imaging³⁹, enabling direct atomic imaging of Rh atoms. In the HAADF STEM images, the point-to-point resolution was approximately 80 pm after Cs correction, and the angular range of the annular detector was 68–280 mrad. All STEM images were collected on a high-resolution (2k×2k) charge-coupled device camera (UltraScan 1000, GATAN) at 80–200 kV. Simulations of HAADF STEM images were performed using MacTempasX software (Total Resolution). The parameters for the simulation were set based on our experimental conditions and using a crystal thickness of 4 nm. For STEM EELS at 80 kV, energy dispersion was set as 0.25 eV/ch and the full-width at half-maximum of the zero-loss peak in vacuum was 1.0 eV. The convergence and collection semi-angles were 19 and 26 mrad, respectively. Digital Micrograph software (GMS 3.2, GATAN) was used for image recording and processing, including Fourier filtering.

XRD characterization. To characterize the crystal structures, XRD analysis was performed on a Rigaku D/MAX-2500H system employing Cu K α radiation. The collected data were analysed by pattern fitting using HighScore Plus software.

X-ray absorption spectroscopy measurements and data processing. X-ray absorption fine structure (XAFS) measurements were made at the 8C nano-probe XAFS beamline (BL8C) of Pohang Light Source (PLS-II) in the 3.0 GeV storage ring, with a ring current of 300 mA. The X-ray beam was monochromated by a Si (111) double crystal where the beam intensity was reduced by 30% to eliminate higher-order harmonics. The X-ray beam was then delivered to a secondary source aperture where the beam size was adjusted to 0.3 mm (v) × 1 mm (h). A high voltage (3,000 V) was applied to ionization chambers filled with N₂/Ar mixture gases to detect X-ray intensity. XAFS spectra were collected in both transmission and fluorescence modes. The obtained spectra were processed using Demeter software. Extended X-ray absorption fine structure (EXAFS) spectra were fitted in a Fourier-transform range of 3–11 Å⁻¹ with a Hanning window applied between 1 Å and 3 Å. The amplitude reduction factor (S_0^2) was set to 0.7 during the fitting.

Photocatalyst studies. *Photocatalytic activity measurements.* Photocatalytic hydrogen generation was measured in a gas-closed system with a quartz cell reactor. TiO₂ powder (5 mg) was dispersed by sonication in an 80 ml solution of water and methanol (volume ratio of 3:1), in which methanol acts as a hole scavenger. After evacuation with Ar gas for 20 min, the quartz cell reactor containing the sample was irradiated by a Xe lamp (MAX-302, Ashai Spectra). The light intensity was measured with a thermophile sensor (818P-001-12, Newport) and fixed at 100 mW cm⁻² by controlling the distance between the reactor and lamp. The reactor was fan-cooled to prevent the light irradiation from increasing the reactor's temperature. The amount of hydrogen gas was determined by gas chromatography (iGC7200, DS Science) and a thermal conductivity detector. AQEs were measured using different bandpass filters (20BPF10-340 and 20BPF10-360, Newport), and the light's incident power was measured using an ultraviolet silicon detector (918D-UV-OD3R, Newport). AQEs were defined as

$$\text{AQE} = 2N_{\text{H}_2}/N_{\text{p}} \quad (1)$$

where N_{H_2} is the number of generated hydrogen molecules and N_{p} is the number of incident photons. For H₂ evolution experiments, materials were heat-treated at 950 °C to increase the crystallinity.

Characterization of photoactivated Cu/TiO₂. A film-type sample was prepared for spectroscopic characterization of Cu/TiO₂. A slurry of Cu/TiO₂ and polyvinylidene fluoride binder dissolved in *N*-methyl-1,2-pyrrolidone was cast on various substrates (PET and Kapton polyimide films) and dried overnight in a vacuum oven. Each sample was dipped in a water/methanol solution and irradiated with light for 10 min in an Ar environment to photoactivate the sample. The reflectance of the film was measured using a UV–visible/near-infrared spectrophotometer with an integrating sphere (V-770, JASCO). Photoluminescence spectra of the film were recorded at room temperature using an Edinburgh Instruments FLS 980 spectrofluorimeter. The excitation wavelength was 300 nm, the scanning speed was 1,200 nm min⁻¹ and the widths of the excitation and emission slits were both 5.0 nm. XANES measurements were performed in fluorescence mode to characterize the photoactivation. Cu K-edge spectra were measured before and after 10 min of light irradiation. After light irradiation, the photoactivated

Cu/TiO₂ film (Kapton film) was placed in a closed cell on the incoming beam path. The cell was attached to an Ar flow apparatus to maintain the Ar environment throughout the XANES measurement. EPR measurements were carried out at 5.7 K using a Bruker EMX plus 6/1 spectrometer operating in the X-band (9.64 GHz) and 100 kHz magnetic field modulation (modulation amplitude, 10 G) equipped with a dual-mode cavity (ER 4116DM). The temperature was controlled using an Oxford Instrument ESR900 liquid He cryostat with an Oxford ITC 503 temperature controller. Spectra were recorded at 0.94 mW microwave power. Five scans were added for each spectrum. For EPR measurements, Cu/TiO₂ powder was dispersed in aqueous methanol solution (5 mg ml⁻¹). Aqueous methanol solution dispersions were examined in sealed quartz tubes after Ar bubbling for the 'before photoactivation sample'. Light was irradiated onto the sealed quartz tube with a Xe lamp for 30 min for the 'after photoactivation sample'. For the 'after regeneration sample', O₂ gas was purged to the 'after photoactivation sample' for 30 min. All quartz tubes were frozen and stored at 77 K using liquid nitrogen before EPR measurements.

Computational details of DFT analysis. *Geometry optimization and characterization of electronic structure.* During DFT calculations, geometry optimizations were performed using the spin-polarized Perdew–Burke–Ernzerhof (PBE) exchange–correlation functional⁴⁰ and the project augmented wave (PAW) method^{41,42}, which are implemented in the Vienna ab initio Simulation Package (VASP) 5.4.1^{43–46}. The structures were optimized until the energy difference of the last two steps became 1 × 10⁻³ eV, and a Monkhorst–Pack 2 × 6 × 1 k-grid was used for surface calculations. We then performed single-point calculations using the PBE-optimized geometries by employing the recent version of the Heyd–Scuseria–Ernzerhof (HSE) hybrid functional⁴⁵ to obtain reliable electronic structures^{46,47}.

Geometry optimization of various configurations. The single atom catalyst formation energies of various configurations were calculated by using 2 × 1 supercell of anatase (101) surface. The kinetic energy cutoff for a plane wave was set to 450 eV. The single atom catalyst formation energy (E_p) is defined as the sum of the binding site preparation energy (E_p) and the single atom binding energy (E_B).

The binding site preparation energy (E_p)⁴⁷ is defined as the defect formation energy of TiO₂ from the elimination of one Ti atom:

$$E_p = E_{\text{tot}}[\text{Ti}_{1-x}\text{O}_2] - E_{\text{tot}}[\text{TiO}_2] - (-\mu_{\text{Ti}})$$

The chemical potential of Ti, μ_{Ti} , is given with respect to the energy of its hexagonal close-packed bulk metal Ti:

$$\mu_{\text{Ti}} = E_{\text{tot}}(\text{Ti}) + \Delta\mu_{\text{Ti}}$$

The chemical potential of O is given with respect to the energy of an O₂ molecule:

$$\mu_{\text{O}} = 1/2E_{\text{tot}}(\text{O}_2) + \Delta\mu_{\text{O}}$$

The chemical potentials of Ti and O should satisfy the growth condition of TiO₂:

$$\Delta\mu_{\text{Ti}} + 2\Delta\mu_{\text{O}} = \Delta H_f(\text{TiO}_2)$$

The chemical potentials of Ti and O should satisfy the growth limitation condition of the phase boundaries between TiO₂ and Ti₂O₃:

$$\begin{aligned} \Delta\mu_{\text{Ti}} + 2\Delta\mu_{\text{O}} &= \Delta H_f(\text{TiO}_2) = -9.25 \text{ eV (O rich)} \\ 2\Delta\mu_{\text{Ti}} + 3\Delta\mu_{\text{O}} &= \Delta H_f(\text{Ti}_2\text{O}_3) = -14.62 \text{ eV (O poor)} \end{aligned}$$

where $\Delta H_f(\text{TiO}_2)$ and $\Delta H_f(\text{Ti}_2\text{O}_3)$ are the DFT-based formation energies of TiO₂ and Ti₂O₃, respectively. Considering the experimental condition, all of the single atom catalyst formation energies were calculated under the oxidizing (O rich) condition where $\Delta\mu_{\text{O}} = 0$ and $\Delta\mu_{\text{Ti}} = -9.25$ eV.

The single atom binding energy (E_B) is defined as the energy that is necessary to introduce one Cu atom

$$E_B = E_{\text{tot}}[\text{Cu/TiO}_2] - E_{\text{tot}}[\text{Ti}_{1-x}\text{O}_2] - E_{\text{atom}}[\text{Cu}]$$

Geometry optimization and characterization of the electronic structure of Cu/TiO₂. Characterization of electron localization and reorganization was performed by using a 1 × 1 unit cell of anatase (101) surface. The kinetic energy cutoff for the plane wave was set to be 500 eV. The band-decomposed partial charge density was visualized using XCrysDen 1.5.60⁴⁸. The core-level shift of Cu 2p states was calculated based on the initial state approximation.

Data availability

All data are available in the main text or in the Supplementary Information.

References

- Liu, H. et al. Crystallinity control of TiO₂ hollow shells through resin-protected calcination for enhanced photocatalytic activity. *Energy Environ. Sci.* **8**, 286–296 (2015).
- Pennycook, S. J. & Jesson, D. E. High-resolution incoherent imaging of crystals. *Phys. Rev. Lett.* **64**, 938–941 (1990).
- Perdew, J. P., Burke, K. & Ernzerhof, M. Generalized gradient approximation made simple. *Phys. Rev. Lett.* **77**, 3865–3868 (1996).
- Blöchl, P. E. Projector augmented-wave method. *Phys. Rev. B* **50**, 17953–17979 (1994).
- Kresse, G. & Joubert, D. From ultrasoft pseudopotentials to the projector augmented-wave method. *Phys. Rev. B* **59**, 1758–1775 (1999).
- Kresse, G. & Hafner, J. Ab initio molecular dynamics for open-shell transition metals. *Phys. Rev. B* **48**, 13115–13118 (1993).
- Kresse, G. & Hafner, J. Ab initio molecular-dynamics simulation of the liquid-metal–amorphous-semiconductor transition in germanium. *Phys. Rev. B* **49**, 14251–14269 (1994).
- Kresse, G. & Furthmüller, J. Efficiency of ab-initio total energy calculations for metals and semiconductors using a plane-wave basis set. *Comput. Mater. Sci.* **6**, 15–50 (1996).
- Kresse, G. & Furthmüller, J. Efficient iterative schemes for ab initio total-energy calculations using a plane-wave basis set. *Phys. Rev. B* **54**, 11169–11186 (1996).
- Matsubara, M., Saniz, R., Partoens, B. & Lamoen, D. Doping anatase TiO₂ with group V-b and VI-b transition metal atoms: a hybrid functional first-principles study. *Phys. Chem. Chem. Phys.* **19**, 1945–1952 (2017).
- Kokalj, A. Computer graphics and graphical user interfaces as tools in simulations of matter at the atomic scale. *Comp. Mater. Sci.* **28**, 155–168 (2003).